

Influence of the elliptical and circular orifices on the local heat transfer distribution of a flat plate impinged by under-expanded jets

Ravish Vinze¹ · M. D. Limeye² · S. V. Prabhu³

Received: 10 March 2016 / Accepted: 15 August 2016 / Published online: 13 September 2016
© Springer-Verlag Berlin Heidelberg 2016

Abstract Experimental study is carried out to explore the influence of nozzle profile on heat transfer for underexpanded impinging jets. Circular and elliptical orifices are used to generate underexpanded jets for underexpansion ratio ranging from 1.25 to 2.67. The supply pressure maintained in the present study ranges from 2.36 to 5.08 times the ambient pressure. IR thermal imaging camera is used to measure surface temperature of thin foil at different nozzle to plate distances. Shadowgraph and pressure distribution are used to understand the flow structure and distribution of circular and elliptical nozzle. It is observed that plate shock and pressure distribution over the plate have significant influence on the local heat transfer. The performance of the circular orifice is far better at lower z/d . The axis switching is observed for an elliptical orifice. Correlation for local heat transfer predicts Nusselt number comparable within 15 % of experimental results.

List of symbols

A	Exit area of the orifice, m^2
C_p	Specific heat of air at constant pressure, $kJ/kg\ K$
c	Velocity of sound, m/sec
D	Diameter meter of the supply pipe, m
d	Equivalent diameter of orifice, m
h	Heat transfer coefficient, W/m^2K
I	Current, A
k	Thermal conductivity of air, W/mK

l	Length of pipe, m
\dot{m}	Mass flow rate, kg/sec
M	Design Mach number, $M = U_\infty/c$
Nu	Nusselt number, $\left(\frac{hd}{k}\right)$
Nu_{avg}	Average Nusselt number
Nu_o	Nusselt Number at the stagnation point
NPR	Nozzle pressure ratio (P_s/P_∞)
P_o	Supply pressure, Pa
P_∞	Ambient pressure, Pa
P_e	Nozzle exit pressure, Pa
p	Perimeter, m
Pr	Prandtl number, $(\mu C_p/k)$
q	Heat transfer rate, W/m^2
q_{conv}	Heat carried out by convection from impinging jet, W/m^2
q_{nat}	Heat carried out by convection from back side of plate, W/m^2
q_{joule}	Total heat supplied, W/m^2
q_{loss}	Heat loss by radiation and convection from the plate, W/m^2
$q_{rad(b)}$	Heat loss by radiation from the back side, W/m^2
$q_{rad(f)}$	Heat loss by radiation from the front side, W/m^2
R	Recovery factor
r	Radial distance from the stagnation point, m
Re	Reynolds number, $(\rho U_\infty d/\mu = 4\dot{m}/\pi \mu d)$
T_{aw}	Adiabatic wall temperature, K
T_{aw}	Adiabatic wall temperature, K
T_d	Jet dynamic temperature, K
T_i	Jet initial temperature, K
T_{j0}	Jet total temperature, K
T_{js}	Jet static temperature, K
T_{jd}	Jet dynamic temperature, K
T_w	Wall temperature, K
U_∞	Velocity, $(U_\infty = \frac{\dot{m}}{A\rho})$, m/sec
V	Voltage, V

✉ S. V. Prabhu
svprabhu@iitb.ac.in

¹ Department of Mechanical Engineering, DIAT, Pune, India

² R & D E (E), DRDO, Pune, India

³ Department of Mechanical Engineering, Indian Institute of Technology, Bombay, Powai, Mumbai 400 076, India

z Nozzle to plate distance, m

Greek symbol

γ Specific heat ratio

μ Viscosity of fluid, Pa.s

ρ Density of fluid, kg/m³

1 Introduction

Heat transfer, as it is a very common phenomenon is day to day life. It is very important to work on improving methods of heat transfer. Jet impingement is a common technique to enhance heat transfer which widely come in application like in glass manufacturing industries, paper and textile mills, Steel manufacturing industries (billet and bloom mills) and chemical industries uses these methods at various stages of manufacturing. In defense and space exploration, in application like missile and rocket exhaust impingement on deflector plate, navigation in space, turbine blade cooling and engine component cooling of gas turbine, jet impingement is extensively used.

The heat transfer due to under-expanded jet impingement has been pursued extensively in the literature by many researchers in the past covering flow dynamics through shadowgraph and the shock structures for wide range of pressure ratios. Henderson [1] and Donaldson and Snedeker [2] studied the flow field and the behaviour of impinging jet originating from a circular convergent nozzle using schlieren photography, surface flow visualization, velocity and surface pressure measurements. Three types of jet flow like subsonic jet, moderately under-expanded jet, and highly under-expanded jet from Mach number 1.8 to 3.57. The heat transfer at stagnation point is found to be dependent upon the velocity gradient in radial direction from stagnation point calculated based on pressure variations. For highly underexpanded jets, flow separation is observed just at the edge of stagnation point for low nozzle to plate distances.

Lamont and Hunt [3] studied the flow pattern of under-expanded jets mainly in the impingement zone for the perpendicular and the inclined target plates (inclinations between 90° and 30°). It is observed that because of multiple shock waves interactions the maximum pressure on inclined plate can be very greater than that for flat plate. Addy [4] has studied the effects of the sonic nozzle geometry on the onset, diameter, and location of the Mach disk in the moderately under-expanded jet. During this study, a contoured converging nozzle, four conically converging sharp edged nozzles, and a sharp edged orifice have been tested. It has been concluded that the Mach disk diameter is influenced strongly by nozzle geometry and weakly by the convergence angle. However, the location of the Mach

disk is relatively independent of the nozzle geometry and convergence angle. Mehta and Prasad [5], Alvi et al. [6] and Inman et al. [7] investigated supersonic free jets (over-expanded and underexpanded) through the numerical simulation and experimentally using convergent–divergent nozzles for the Mach numbers ranging from 1.31 to 3.1 for the ratio of exit pressure to the ambient pressure from 0.4 to 5. Effects of Mach number and the exit to ambient pressure ratio on shock cell lengths are investigated with the help of schlieren pictures and density contour plots. Inman et al. [7] interpreted the surface pressure profiles using the planar laser-induced fluorescence which also exhibited the flow structures for the under-expanded supersonic and sonic free and impinging jets issued from convergent and convergent–divergent nozzles. These experiments were conducted in sub-atmospheric region.

Thangadurai and Das [8] have studied the characteristics of high Mach number compressible jets experimentally using high-speed laser sheet-based flow visualization. The formation mechanism and the evolution of counter rotating vortex ring formed ahead of the primary vortex ring are studied in details for Mach number ($M = 1.7$). It is reported that the strength of embedded shock and the generating jet length play decisive role in formation of counter rotating vortex ring. The diameter of the vortex ring increases during its formation as the Mach number increases. Noise produced during normal impingement of a compressible vortex ring on a flat surface is studied in the Mach number range of 1.31–1.55 by Thangadurai and Das [9] It is reported that the impingement noise results in the fluctuating pressure due to deformation and stretching of the vortex ring, formation and growth of a secondary wall vortex ring, lifting-off of the primary-secondary vortex ring pair.

Rajapukeran [10], Yaga et al. [11], Jothi and Srinivasan [12] and Srinivasan et al. [13] have investigated underexpanded jets originated from non-circular nozzle like—triangular, rounded triangular, elliptical, square and rectangular. Rajapukeran [10] studied a elliptical nozzle for aspect ratios ranging from 1.4 to 5 for the pressure ratio of 2.9–20.3. It is reported that the locations of the axis switching for the supersonic nozzles are much closer to the nozzle exit than for the subsonic nozzles and that the locations are strongly dependent upon the pressure and aspect ratios. Yaga et al. [11] compared the converging circular (of 10 mm diameter) and rectangular nozzles (aspect ratio of 3) for under-expanded impinging jets (pressure ratios of 3 and 4.5), and showed that the stagnation temperature is dependent on the pressure ratio and z/d . An experimental study of acoustic characteristics of non-circular jets carried out by Jothi and Srinivasan [12]. Srinivasan et al. [13] compared the noise characteristics of underexpanded jets issued from the rectangular and elliptical disk nozzles of various aspect ratios. It is found that the aspect ratio plays

an important role in noise suppression applications i.e., the lower aspect ratios seem to be advantageous than the higher aspect ratios, and that the acoustic characteristics of higher and lower aspect ratio jets of elliptic and rectangular shapes are entirely different.

Studies pertaining to the heat transfer for the under-expanded jet impingement are reviewed here. Rahimi et al. [14] presented the experimental data for the heat transfer on a flat surface impinged by an under-expanded jet issued from a convergent nozzle of 12.7 mm diameter for various pressure ratios (P_0/P_∞) ranging from 1.68 to 5.08 for nozzle to plate spacing ranging from 3 to 40. They reported that the lower nozzle-to-plate spacing, the degree of under expansion plays a significant role in determining the heat transfer. They concluded that the Nusselt number as a function of Reynolds number is inadequate in compressible flows and the dimensional analysis showed that the nozzle Mach number or pressure ratio should be included in case of supersonic flows. Kim et al. [15, 16] and Yu et al. [17] conducted an experimental investigation of the impingement of under-expanded, axisymmetric and supersonic and sonic jets for nozzle pressure ratios ranging from 2.84 to 8.62. The surface pressure and the adiabatic wall temperature distributions on the flat plate are reported along with visualization of shock structures to study the heat transfer augmentation at the stagnation point and at the jet periphery at small nozzle-to-plate distances. It is found that turbulence diffusion from the shear layers around the jet edge and sonic surfaces into the jet core region induced higher heat transfer rates while existence of low temperature region along the jet periphery and at the stagnation point attributed to vortex-induced temperature separation and shock-induced temperature separation (or existence of the recirculation bubble). Ramanujachari et al. [18] carried out heat transfer experiments with high velocity and high temperature rocket exhaust gases generated by burning nitramine based propellant. On the basis of the Nusselt number distribution, it is inferred that the flow field is influenced by the mixing of jet fluid as the nozzle to plate distance is increased. Maximum Nusselt number values for the supersonic jet are an order of magnitude more than that of the subsonic jet.

Number of research works is carried out to understand the flow structures as a result of the shocks and its interaction with the mean flow, and the stagnation bubble in the supersonic jets. Due to complexity of flow, each work is carried out with some single specific purpose. It is reported that the jet spreading and mixing for the non-circular jets are more vigorous than compared to circular orifice and that noise generation is low for the non-circular orifice than the circular orifice by Rajakuperan [10]. However, there are a few works solely devoted to the heat transfer due to impingement. The impingement heat transfer is an outcome

of the mean flow dynamics and its manifestation in the vicinity of the impingement surface. The literature available on the heat transfer is devoted to circular jets issued from the convergent nozzles or convergent-divergent nozzles. Hence, the objectives of present study are as follows-

- To study the local heat transfer due to impinging under-expanded jet originating from circular and elliptical orifice.
- To correlate the flow structure captured in shadow-graphs and pressure distribution with the local heat transfer distribution.

2 Experimental apparatus and data reduction

A schematic layout of the test facility for heat transfer measurement is shown in the Fig. 1a. Compressor (capacity 50 gm/s at 10 bar) supplies compressed air of metered quantity through pressure regulator and calibrated venturi meter. The air filter and the pressure regulator are installed

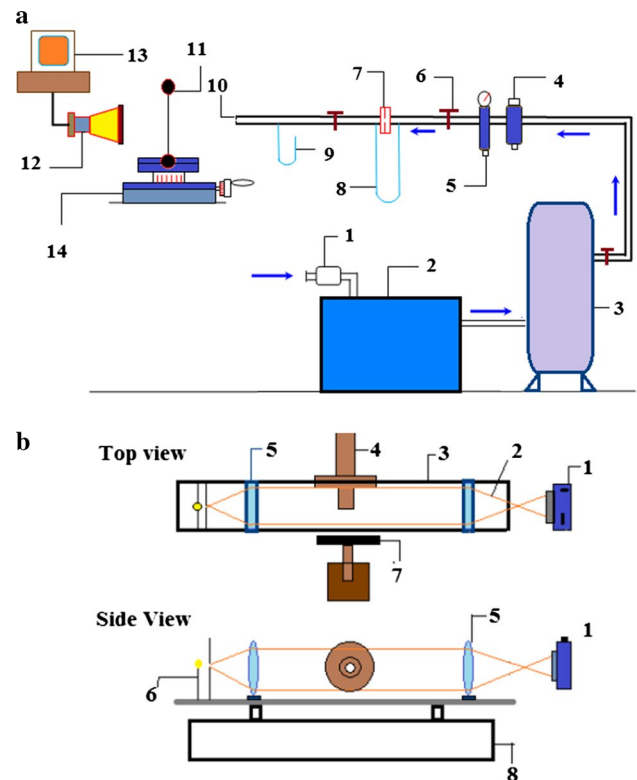


Fig. 1 Layout of experimental setup. **a** (1) Air filter (2) Air compressor (3) Air receiver (4) Air filter (5) Pressure regulator (6) Needle valves (7) Venturi meter (8) Differential manometer (9) Simple manometer (10) Orifice (11) Impingement plate assembly (12) Infrared camera (13) Computer (14) Traverse system. **b** (1) Camera (2) Light rays (3) Traverse system (4) Nozzle (5) Lenses (6) Light source (7) Impingement plate (8) Table

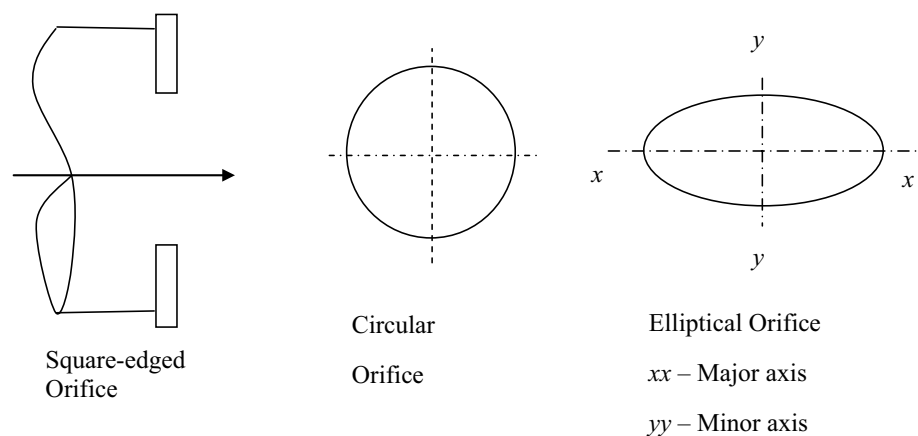
Table 1 Dimensional details of orifices

Type of orifice	Size, mm	Cross sectional area, mm ²	Perimeter	Equivalent diameter, mm
Circular	5.8	26.42	18.16	5.8
Elliptical	8.4 and 4.2	27.71	20.35	5.93

upstream of the venturi flow meter. The flow rate to the test section is regulated by the valve located downstream of the venturi flow meter. The elliptical orifice is made out of 3 mm steel plate having a major diameter of 8.4 mm and a minor diameter of 4.2 mm. These dimensions are so chosen that the equivalent diameter based on the cross sectional area is same as for the circular orifice ($d = 5.8$ mm). The equivalent diameter is calculated using the Eq. 1 and dimensional details of orifices are given in Table 1.

$$d_e = \sqrt{\frac{4A}{\pi}} \quad (1)$$

Figure 2 shows sketch of circular and elliptical orifice made of 3 mm thick plate have square-edged sections and no chamfering is provided at the inlet and outlet. The orifice plate is welded on a pipe of 25 mm ID having a length over 1.25 m. The length of the pipe ensures that there is no disturbance transfer to the end of supply pipe where orifice is fixed. The major axis of the elliptical orifice is parallel to the longitudinal axis of the target plate. Experimental parameters for both the orifices at various pressure ratios are summarized in Table 2. It is observed that the coefficient of discharge is almost independent of the nozzle pressure ratios considered under study. The coefficient of discharge values for the elliptical orifice is slightly higher than the circular orifice, but within the range of experimental uncertainty. Similar experimental setup is also used in our previous studies as reported by Meena et al. [19] and Vinze et al. [20].

Fig. 2 Experimental configuration of orifices

The impinging plate of dimensions 143×45 mm (0.08 mm thick stainless steel foil) used in the experiment as target deflector plate. The plate is clamped tightly between two copper bus bars is connected to AC power supply for heating. Approximately 5 mm of the thin foil on either side is sandwiched between the two copper bars to ensure firm grip. Because of the thinness of foil, lateral conduction is assumed to be negligible since the heat loss is very small compared to the heat flux supplied to the impingement surface and surface provides constant heat flux situation as reported by Lytle and web [21]. The back side of the target surface is painted black using a thin coat of ‘Matte Finish Asian’ paint which provides high emissivity (0.99) surface. The emissivity of surface is calibrated as per the method reported by Katti et al. [22]. The voltage across the target plate is measured by ‘Meco’ digital meter whose ranges and accuracies are of $0-20 \pm 0.5 \% V$. Suitable voltage taps are provided in each of the bus bars. In this experiment, the nozzle used for jet impingement is convergent type (Fig. 1a), The jet air temperature is measured using a Chromel–Alumel thermocouple (K-type) positioned at the inlet of the nozzle. The output of the thermocouple is measured by ‘Meco’ millivoltmeter in the range of 0–2 mV.

For each case, the wall temperature (T_w) of target surface recorded under steady state conditions using the thermal images from the infra-red camera VisIR[®] Ti 200. The Nusselt number (Nu) is calculated based on heat transfer coefficient as given by Eq. 6. To calculate heat transfer coefficient (h), the adiabatic wall temperature (T_{aw}) is taken as the reference temperature. It is that temperature the heat transfer surface assumes when it is in equilibrium with the jet i.e., when there is no heat transfer between the jet and the impingement surface. The thermal images converted to $m \times n$ matrix format which gives the temperature distribution on plate surface. Further processing is executed in MATLAB. The losses from the test plate due to convection and radiation are taken care in calculations of heat loss in

Table 2 Measured performance characteristics of orifices

P_o/P_∞	P_e/P_∞	Circular orifice			Elliptical orifice		
		C_d	\dot{m} (kg/s)	Re	C_d	\dot{m} (kg/s)	Re
2.36	1.25	0.61	0.0081	97,000	0.63	0.0084	100,100
3.04	1.61	0.61	0.0105	125,000	0.62	0.0106	126,000
3.72	1.97	0.60	0.0125	149,000	0.63	0.0132	158,000
4.4	2.32	0.61	0.0151	181,000	0.64	0.0157	188,000
5.08	2.67	0.58	0.0173	205,000	0.61	0.0181	215,000

Eq. 3. The local convective heat transfer coefficient and corresponding Nusselt number in the target surface were estimated based on the following equations.

$$\text{Heat transfer coefficient: } h = \frac{q_{conv}}{T_w - T_{aw}} \quad (2)$$

where: T_w = wall temperature (K), T_{aw} = adiabatic wall temperature (K)

$$\text{Total convective heat transfer: } q_{conv} = q_{joule} - q_{loss} \quad (3)$$

$$\text{Total heat supplied: } q_{joule} = VI/A \quad (4)$$

where: V = supply voltage (V); I = supply current (Amp)
 A = plate area (m^2)

Total heat loss due to natural convection and radiation:

$$q_{loss} = q_{rad(f)} + q_{rad(b)} + q_{nat} \quad (5)$$

$$\text{Nusselt number: } Nu = \frac{hd}{k} \quad (6)$$

where: thermal conductivity of air $k = 0.0262$ (W/m K)

Recovery factor is the ratio of actual rise in temperature of the wall surface to ideal rise in temperature of the air due to deceleration of the jet air approaching the impingement surface. The adiabatic wall temperature measurements are presented in a dimensionless form as recovery factor:

$$R = \frac{T_{aw} - T_{js}}{T_{jo} - T_{js}} = \frac{T_{aw} - T_{js}}{T_{jd}} = 1 + \frac{T_{aw} - T_{j0}}{\frac{U_\infty^2}{2C_p}} \quad (7)$$

$$= \frac{2}{(\gamma - 1)M^2} \left(\frac{T_{aw}}{T_{js}} - 1 \right)$$

$$\text{Jet dynamic temperature: } T_{jd} = \frac{U_\infty^2}{2C_p} = \frac{\left[\frac{\gamma-1}{2} M^2 \right]}{1 + \left[\frac{\gamma-1}{2} M^2 \right]} T_{j0} \quad (8)$$

$$\text{Mach number: } M = \frac{U_\infty}{\sqrt{\gamma RT_{js}}} \quad (9)$$

The under-expansion ratio is determined from the following relation:

$$\frac{P_s}{P_\infty} = \frac{P_e}{P_\infty} \left[1 + \left(\frac{\gamma - 1}{2} \right) M^2 \right]^{\frac{\gamma}{\gamma-1}} \quad (10)$$

The range of experiments covered is given in Table 2. The Reynold number is calculated based on the exit conditions arrived at by assuming the isentropic expansion flow. The values of thermal conductivity (k) and viscosity (μ) of air used in the present study are 0.0262 W/mK and 18.54×10^{-6} Pa.s. The uncertainty in the evaluation of Nusselt number is 3.6 and 4 % for the elliptical and circular orifice respectively calculated based on method reported by Moffat [23]. Similarly the uncertainties in the measurement of coefficient of discharge (C_d), mass flow rate, Reynolds number and recovery factor are calculated as around 4.5, 2.97, 3.4 and 7.3 % respectively.

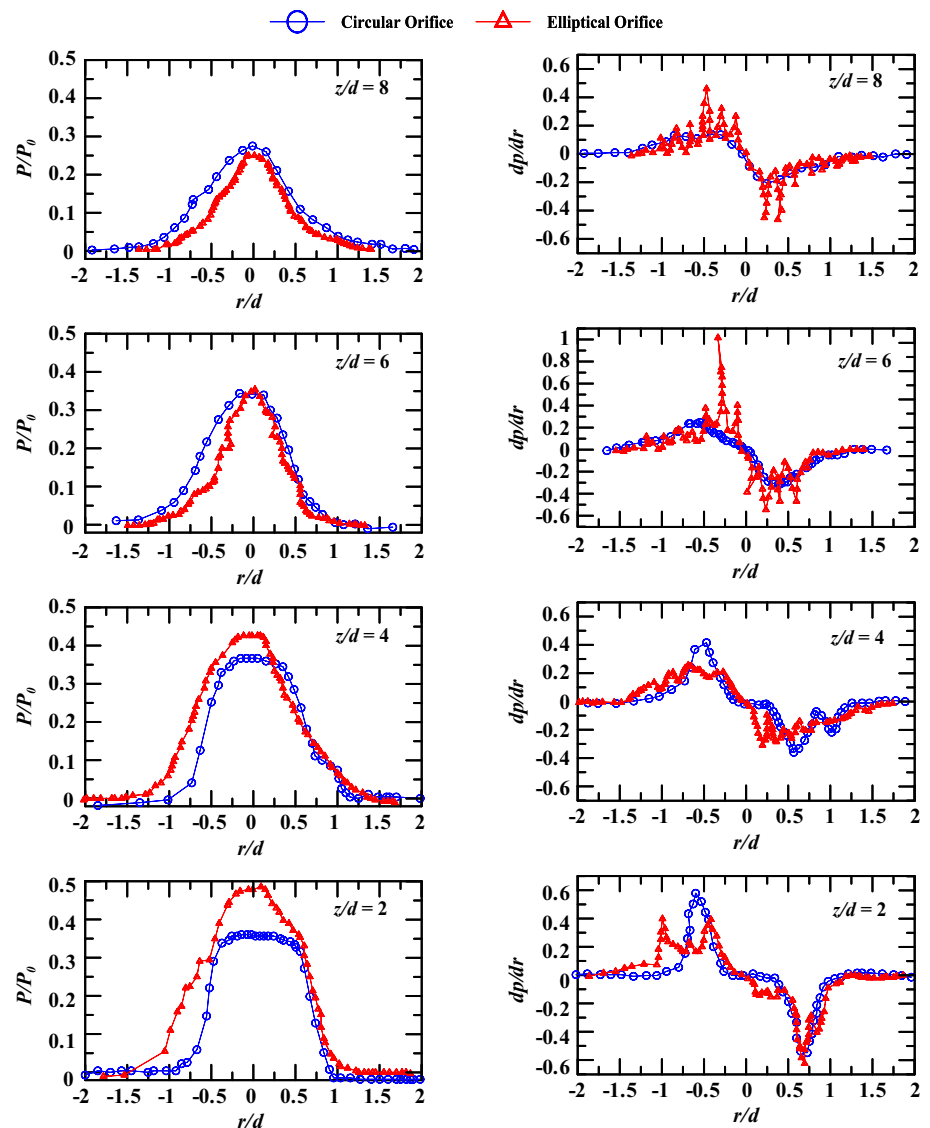
3 Results and discussion

Experiments are conducted to measure local heat transfer and pressure distribution for jets issuing from circular and elliptical orifices. Local Nusselt number and recovery factor for both the orifices are measured for the pressure ratios of 2.36, 3.04, 3.72, 4.4 and 5.08 at different nozzle-to-plate distances ($z/d = 2, 4, 6$ and 8). Shadowgraphs are also captured for both orifice jets at nozzle to plate distances for $z/d = 1-4$ for different NPR.

3.1 Surface pressure distribution

Figure 3 shows the comparison of the surface pressure and its gradient along the radial direction for the circular and elliptical orifices at $z/d = 2, 4, 6$ and 8 for $NPR = 2.36$. The surface pressure is uniform in the jet central region ($\partial p/\partial r \sim 0$ for $r/d \sim \pm 0.16$) for the circular orifice at $z/d = 2$ and it is gradually decreasing away from the stagnation point. As the nozzle to plate distance increases, the uniform pressure distribution region increases ($\partial p/\partial r \sim 0$ for $r/d \sim \pm 0.75$ at

Fig. 3 Comparison of the surface pressure and its gradient for circular and elliptical orifices at $NPR = 2.36$



$z/d = 8$). In the radial direction, pressure drops uniformly and forms bell shaped distribution for circular jets. The surface pressure in the stagnation region is lower for the circular orifice than that for the elliptical orifice at $z/d = 2$ and 4, and it is almost identical at $z/d = 6$ and 8 for both orifices, which may be due to the identical cross sections of the jets. The radial distribution of the pressure gradient for the circular orifice is more gradual and smoother than that for the elliptical orifice, thus indicating smoother velocity distribution across the jet section of the circular orifice for $z/d = 2$ –8. The pressure distribution and the spatial gradient of the pressure indicate the differences in the velocity distribution in the jet sections of the circular and elliptical orifices.

Figure 4 shows the radial distribution of the surface pressure and its gradient for $NPR 3.04$ at $z/d = 2, 4, 6$ and 8 for the elliptical orifice. The pressure distribution is ‘wider’ for $z/d = 2$ than it is at $z/d = 8$ indicating the impact on

the plate took place ‘within’ the potential core region of the elliptical jet. However, For $z/d = 2$, the pressure gradient is very large at the jet periphery as compared to the same for other z/d . Figure 5 shows the surface pressure distribution along the axial direction for the elliptical orifice at $NPR = 2.36, 3.04, 4.4$ and 5.08 and for the circular orifice at $NPR 2.36, 3.72$ and 5.08. The surface pressures in the vicinity of the exit plane of orifice could not be measured due to the deflection of the target plate towards the orifice. The central surface pressure at the exit plane of the circular orifice (e.g., $p/P_0 \sim 0.7$ at $NPR 2.36$) is lesser than the elliptical orifice (e.g., $p/P_0 \sim 0.9$ at $NPR 2.36$) for all NPR , thus it seems to be affected by the changes of profile of orifice. The flow through an orifice is characterised by the ‘vena contracta’ which is formed due to the curvature of the streamlines. The presence of the vena contracta may be estimated from the steeper favourable pressure gradient close

Fig. 4 Comparison of the surface pressure and its gradient for the elliptical orifice at $NPR = 3.04$

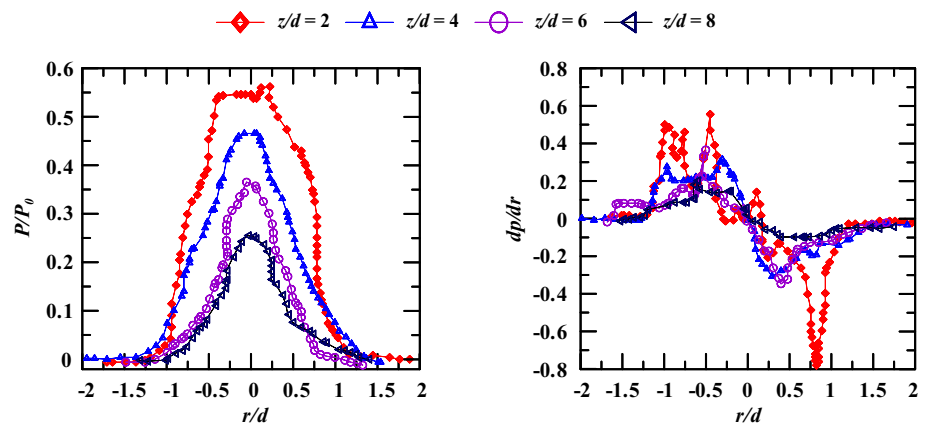
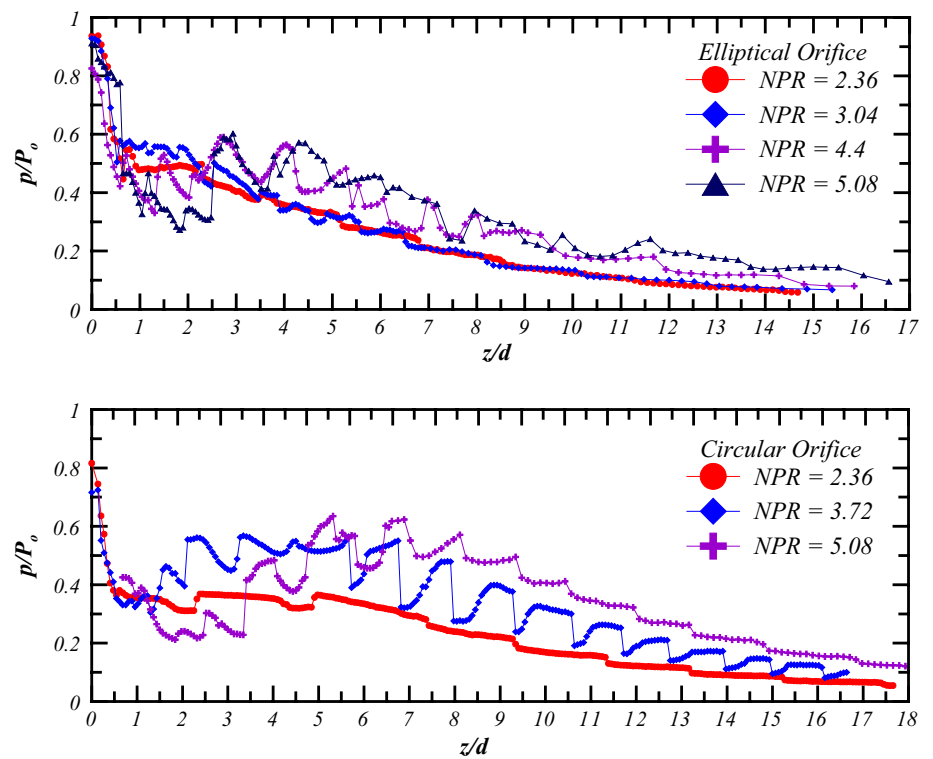


Fig. 5 The surface pressure distribution along the jet axis for the elliptical and circular orifice



to the exit of the orifice. The location of the vena contracta for the circular orifice is almost same which is closer to that reported by Quinn [24] for the turbulent incompressible circular jet (~ 0.25). It may be attributed to the large pressure differential that exists across the cross section of the elliptical orifice due to variation in the curvature radius as shown in the Figs. 3 and 4.

The central surface pressure gradually decreases away from the exit of the orifice for all NPR till the recovery of the pressure is initiated, which may be termed as the initial length of expansion. The length of initial expansion increases with NPR for both orifices e.g., for NPR 2.36,

$z/d \sim 0.5$ for both orifices and, for NPR 5.08, $z/d \sim 1$ and 2 for the elliptical and circular orifices, respectively. It may be noted that the length of the initial expansion is shorter for the elliptical orifice than the circular orifice at higher NPR , (refer Fig. 5, the top two curves for comparison) which may be attributed to the vorticity differences across the section of the orifice affecting the mixing. The vorticity differences exist across the elliptical jet section due to variation in the velocity gradient along the periphery of the jet surface.

For $NPR = 3.72$ and 5.08, the recovery of pressure takes place through a series of compression and expansion processes for the circular orifice. For $NPR = 3.72$, in

case of the circular orifice, the recovery of pressure takes place through the cyclic fluctuation of the surface pressure with increasing magnitudes from $z/d \sim 0.6$ to 2 which may be due to either reflection of the generated expansion waves from the target plate or the oscillations generated by the shock waves as reported by Jothi and Srinivasan [25]

and Iwamoto and Deckker [26]. The shock cell captured in shadow graphs as shown in Figs. 6, 7 and 8 also shows good agreement with this observation. For $NPR = 5.08$, the recovery of pressure is non-uniform which may be due to cyclic compression and expansion of fluid. These compression and expansion processes also indicative of locations of the

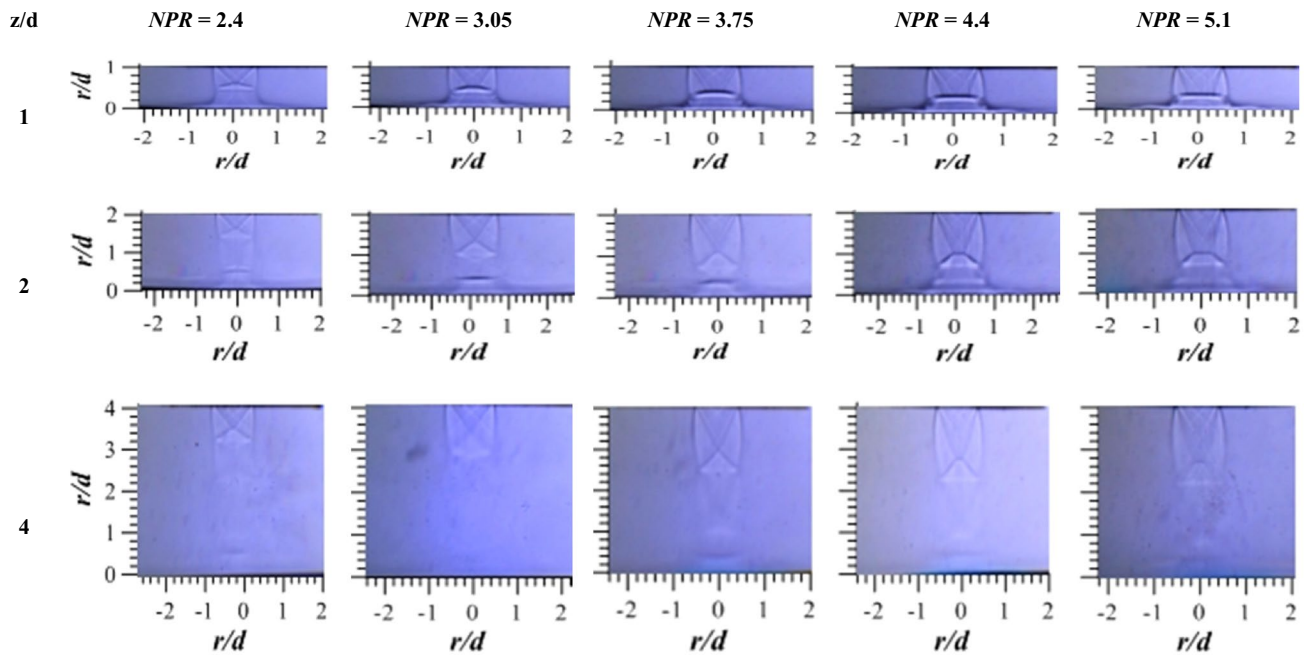


Fig. 6 Jet impingement shadowgraphs for circular orifice

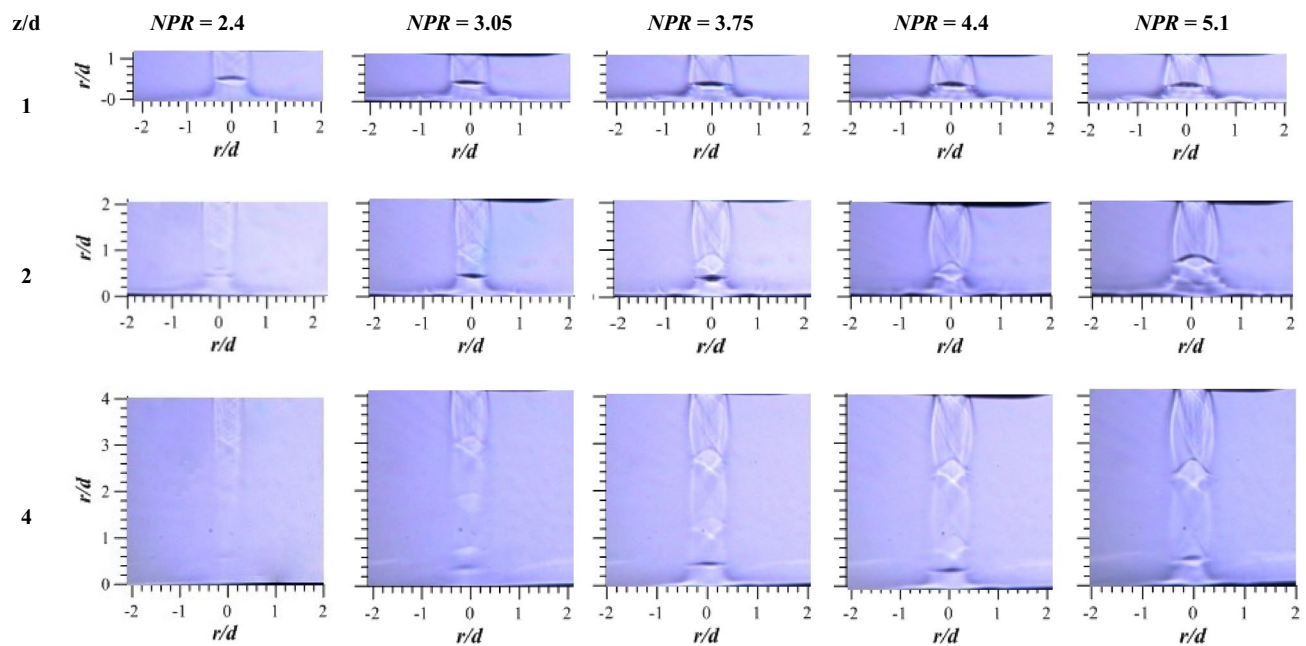


Fig. 7 Jet impingement shadowgraphs when minor axis of elliptical orifice is parallel to the length of test plate at different NPR and z/d

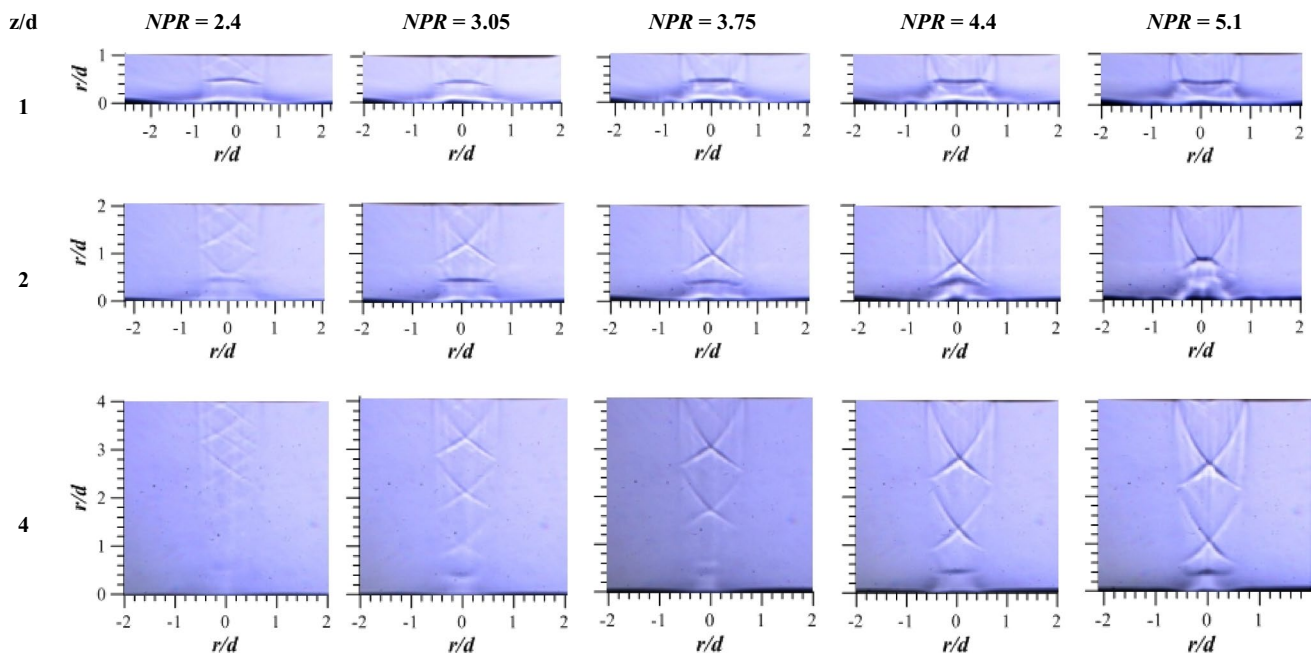


Fig. 8 Jet impingement shadowgraphs when major axis of elliptical orifice is parallel to the length of test plate at different NPR and z/d

shock cell and Mach disk as it is captured in shadow graph study (Figs. 6, 7, 8). In the shock cell region pressure drop is gradual at the end of which Mach disk is formed across which flow changes from sonic to subsonic flow.

3.2 Jet impingement shadowgraph

Figures 6, 7 and 8 show shadowgraphs for impinging circular and elliptical jets. For elliptical jets, shadowgraphs are captured on major and minor axis as it is asymmetric orifice profile. In case of free underexpanded jet, as the compressed fluid originates from nozzle, compressed fluid tries to expand and a constant pressure jet boundary reflects it back inside the jet core. This sudden expansion and compression results in the formation of a shock cell within the jet core. At the end of shock cell Mach disc forms, across with the fluid velocity changes from sonic to subsonic flow. This cycle repeats until fluids compressibility becomes insignificant to produce a shock. The axial pressure distribution confirms this observation as shown in Fig. 5. In case of impinging jets along with shock cell, plate shock (reflected shock) also forms as shown in Figs. 6, 7 and 8. As the NPR increases, shock cell length also increases. From the shadowgraphs, it can be observed that for lower value of NPR ($NPR \leq 3.04$), shock cell is formed before the jet impingement on the plate (for $z/d = 1$). However, for higher NPR ($NPR \geq 3.72$), shock cell is not completely formed for low z/d before impingement. For low NPR ($NPR \leq 3.04$) at $z/d = 4$, plate shock cell structure is

almost insignificant over the plate. While for higher NPR ($NPR \geq 3.72$), shock cell and reflected shock (plate shock) exist even at $z/d = 4$. For circular as well as elliptical jet, the formation of shock cell and plate shock over the flat plate are similar. Except for elliptical jet, shock cell breadth is in proportion to major and minor diameter of orifice. This observation confirms the pressure drop distribution explained in prior discussion (Figs. 3, 4). This distribution plays an important role in guiding local heat transfer over the flat plate. It may be concluded that the pressure and the velocity distribution in the radial and the axial direction are dependent upon the curvature profile of the flow device which in turn, governs the flow structure development in the free jet region.

3.3 Local Nusselt number distribution

Figures 9, 10 and 11 show the local Nusselt number distribution for elliptical (on major and minor axis) and circular orifice jets respectively, at different z/d and for various NPR s. At $z/d = 2$ it is observed that, the Nusselt number distribution is dependent upon the NPR . In the stagnation region, Nusselt number for highly under-expanded jet ($NPR \geq 4.36$) is around 55 % for elliptical and 27 % for circular jet higher than that for the moderately under-expanded jet. The heat transfer rate for the circular orifice is higher, in general, than the elliptical orifice at all z/d . For the moderately under-expanded jets ($NPR \leq 3.72$), the circular orifice (Fig. 11) exhibits better heat transfer rates

Fig. 9 Nusselt number distribution for the elliptical orifice along the minor axis

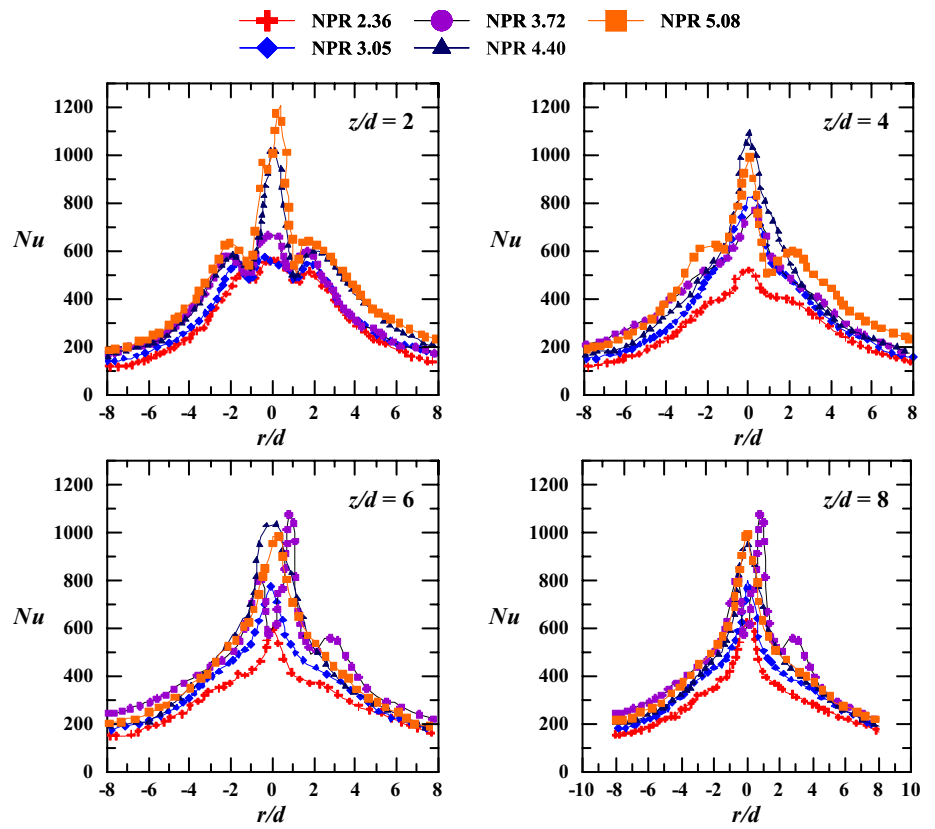


Fig. 10 Nusselt number distribution for the elliptical orifice along the major axis

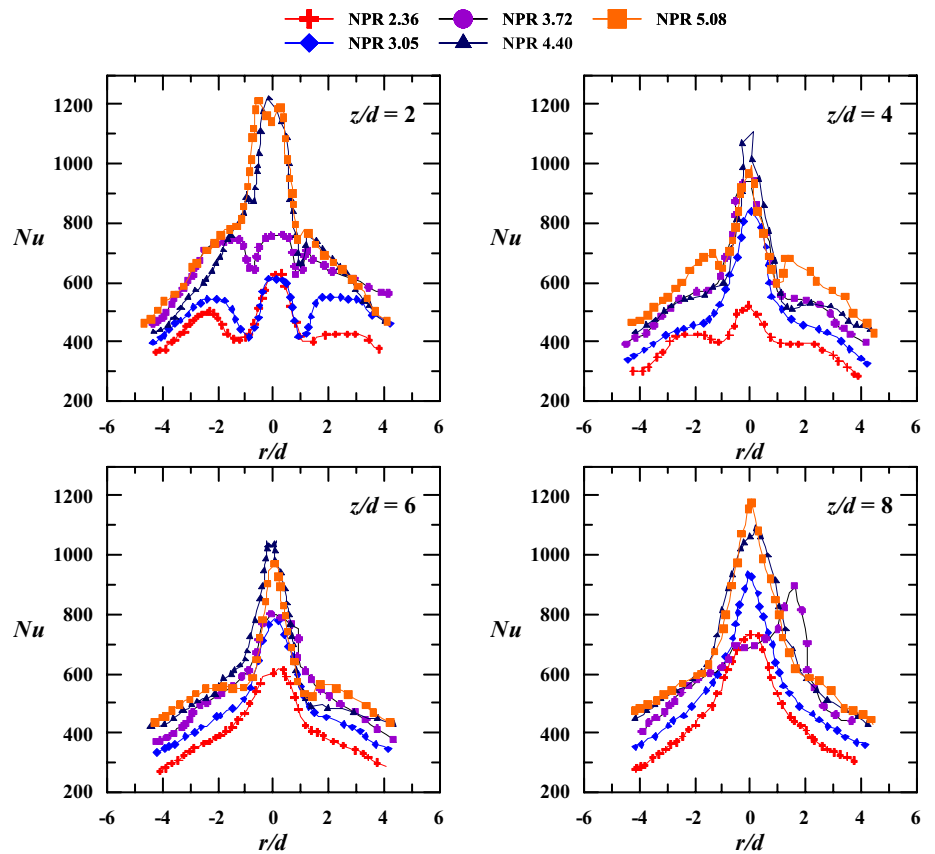
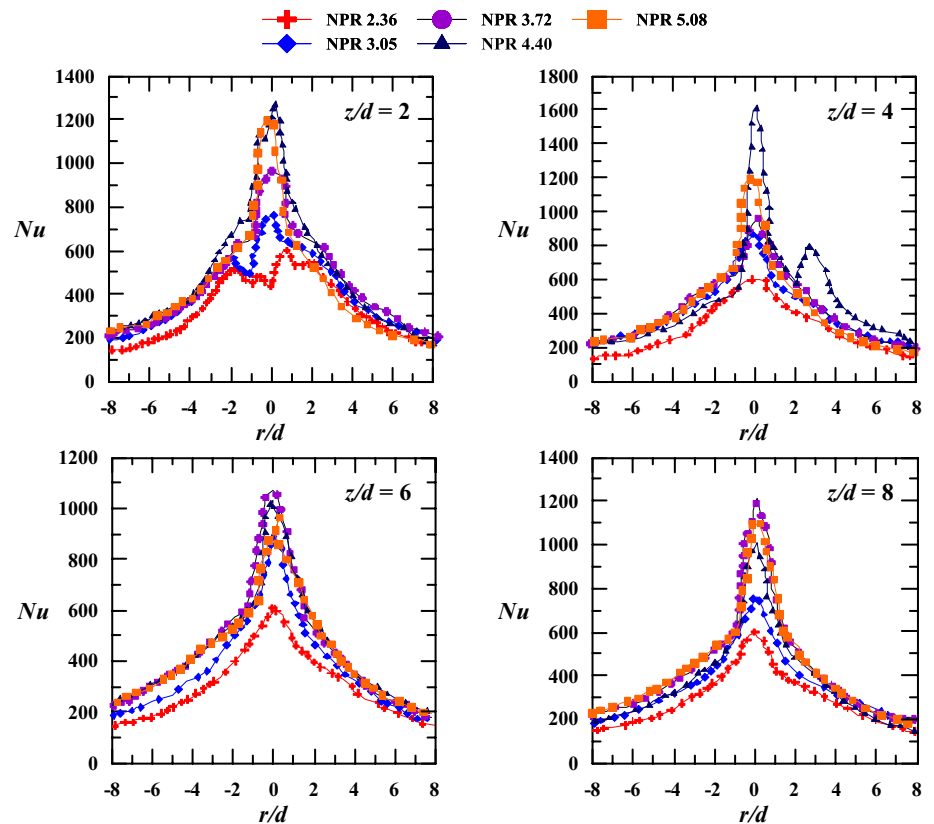


Fig. 11 Nusselt number distribution for the circular orifice

than the elliptical orifice at all z/d except at $z/d = 4$ e.g., at $z/d = 6$ the comparative heat transfer is increased by 35 % with increase in NPR . For the highly under-expanded jets ($NPR \geq 4.36$), the comparative performance of the circular orifice shows downward trend with increase in z/d and NPR viz., at $z/d = 4$, the heat transfer rate at stagnation point decreased by 25 % with increase in NPR from 4.4 to 5.08.

The pronounced secondary maxima is observed for the elliptical orifice at $z/d = 2$ for all NPR . The differences in the Nusselt number distributions along the major axis and minor axis are testimony to the unsymmetrical distribution of heat transfer characteristics of the elliptical orifice. Shadowgraph images also vindicate this observation over major and minor axis (Figs. 7, 8) where plate shocks are observed over the plate. It is observed that when the pressure ratio changes from $NPR = 2.36$ to 3.04 the stagnation Nusselt number is increased by (as an average) 25 % for the elliptical orifice while it is 46 % (as an average) for the circular orifice, and then it is decreased with further increase in NPR . Similarly, as the pressure ratio changes from the moderately under-expanded to highly under-expanded jets i.e. from $NPR = 3.72$ to 5.08, the stagnation Nusselt number is increased by (as an average) 40 % for the elliptical orifice while it is 18 % (as an average) for the circular orifice.

The contour plots (Figs. 12, 13, 14) of Nusselt number for the elliptical orifice can be studied by dividing the total area into three regions viz., stagnation region, transition region and the wall jet region away from the stagnation point. At $z/d = 2$ and 4 for all NPR , the jet core region is of almost circular in shape at highest value of heat transfer and it becomes elliptical at $z/d = 6$ and 8 with major axis aligned vertically, thus indicating ‘axis rotation’ in the core region. The region of jet periphery is characterized by the presence of vortex structures surrounding the core region as reported by Yu et al. [17]. These structures may be in form of semicircular or globular shape at higher value of heat transfer, but separated from the core region by smaller globules of lower Nusselt number at lower z/d for moderately under-expanded jets. In case of highly under-expanded jets, the region immediately surrounding the core region is at a comparatively lower value of heat transfer (as compared with the moderately under-expanded jet). It is observed that the regions of lower Nusselt number are surrounded by the regions of higher Nusselt number. This may be attributed due to vortex ring which surrounds the stagnation region over the plate as also reported by Kim et al. [15, 16] and Yu et al. [17]. At the centre of this vortex ring, higher Nusselt number is observed due to acceleration of fluid flow.

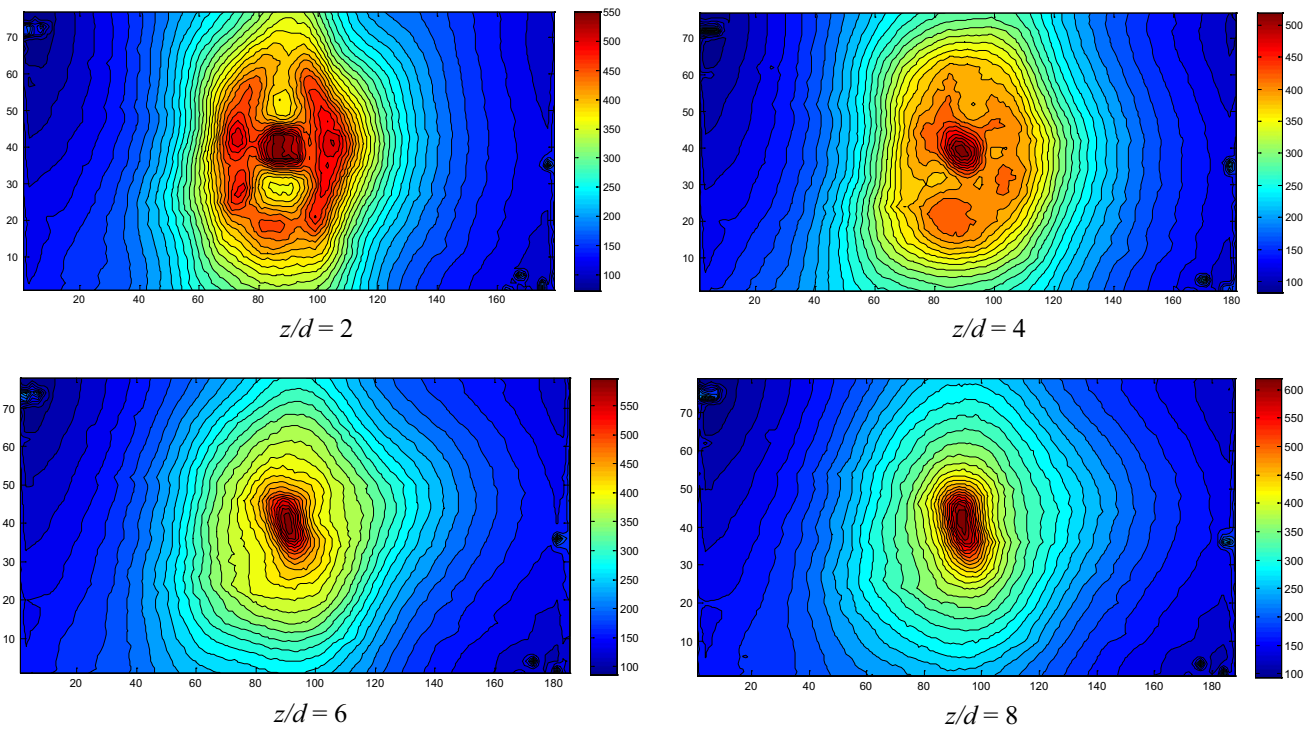


Fig. 12 Contour plots for Nusselt number for the elliptical orifice at NPR 2.36

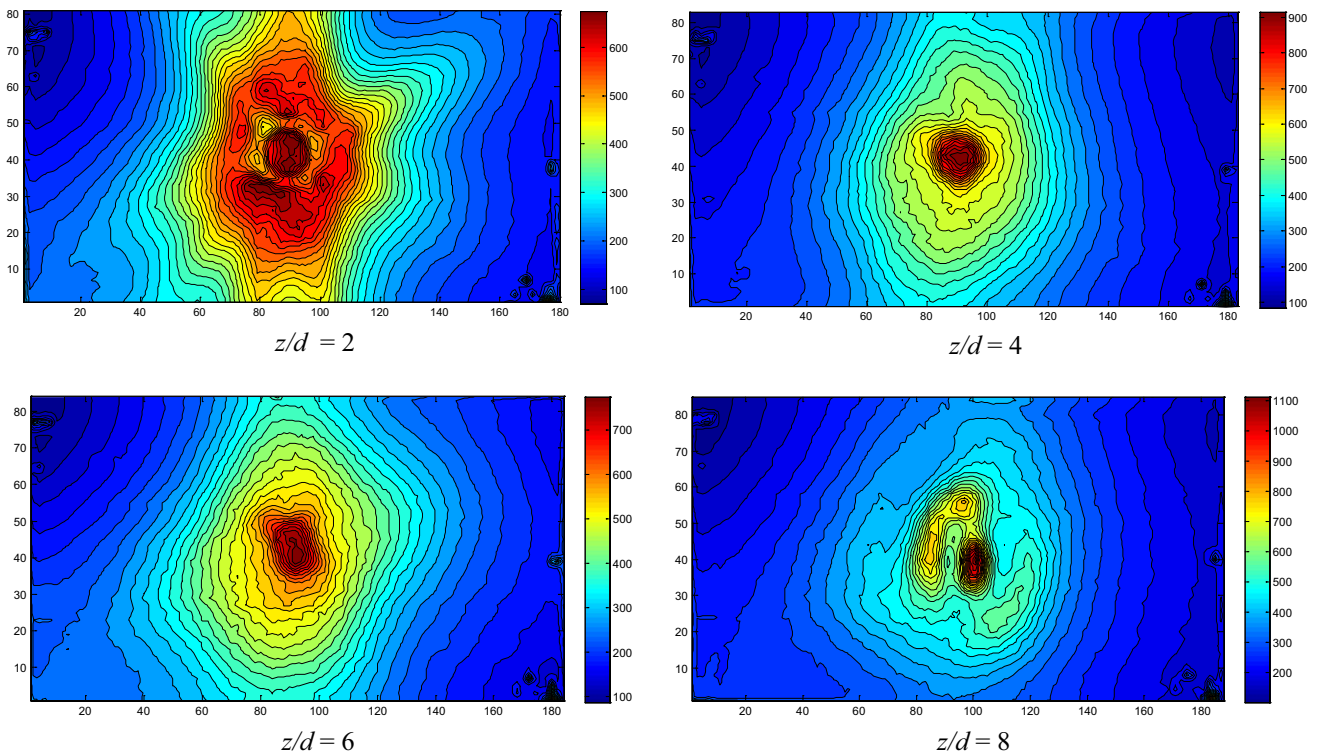


Fig. 13 Contour plots for Nusselt number for the elliptical orifice at NPR 3.72

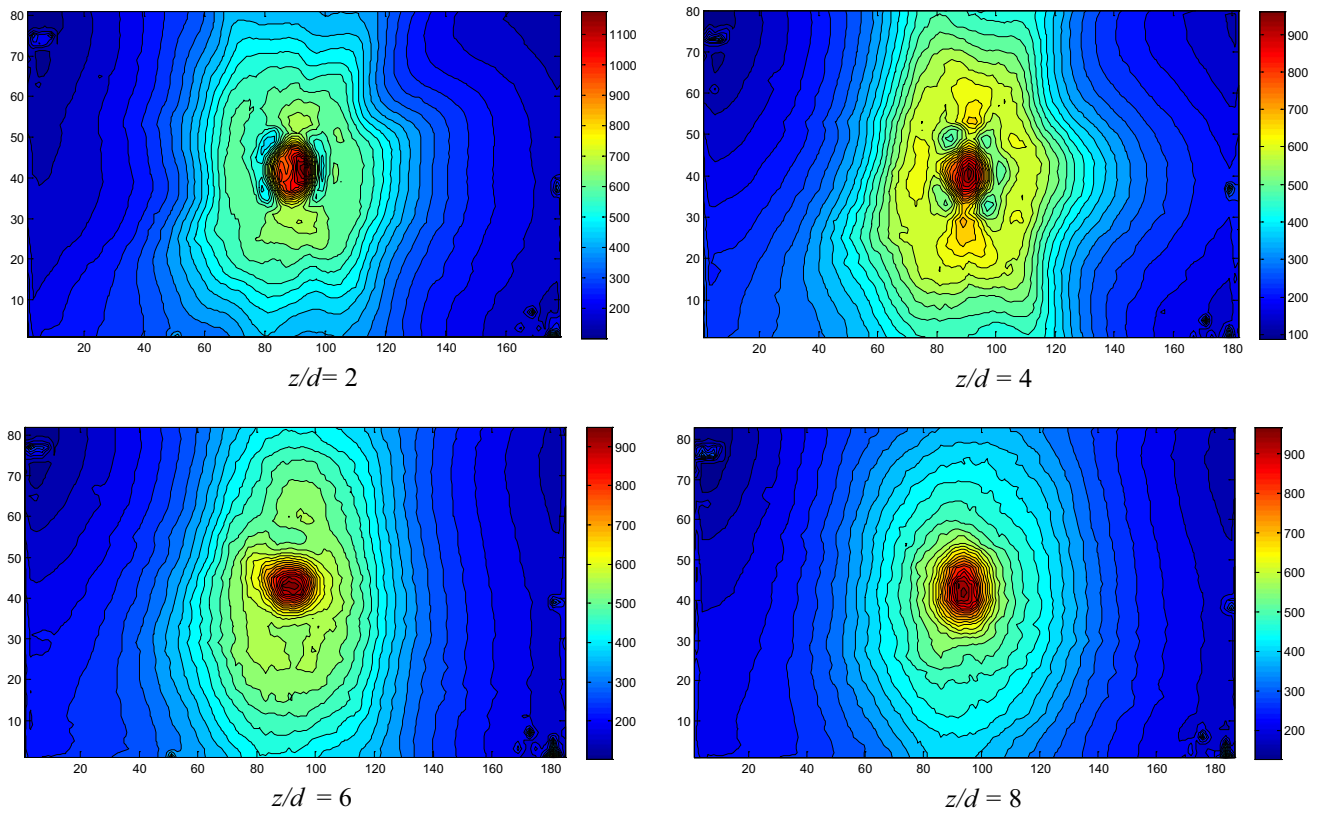
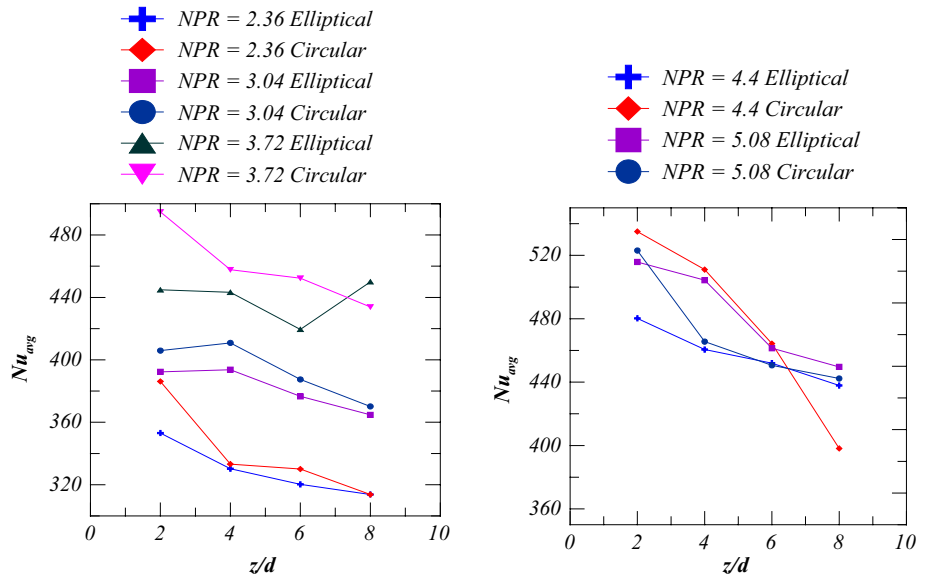


Fig. 14 Contour plots for Nusselt number for the elliptical orifice at *NPR* 5.08

Fig. 15 The average Nusselt number for the circular and elliptical orifices



3.4 Average Nusselt number distribution

Figure 15 shows the variation of the area average Nusselt number at various z/d for all *NPR* for both orifices. The area considered for the averaging of the Nusselt number is $r/d = \pm 4$ since this is area which makes the difference

in the Nusselt number distribution. It is observed that the values of the average Nusselt number for the elliptical orifice are lesser than that for the circular orifice for all *NPR* (except *NPR* 5.08) at almost all z/d . It can be concluded that circular orifice has better performance compared that to elliptical orifice by about 3–4 %.

3.5 Recovery factor distribution

Figure 16 shows the recovery factor distribution in radial direction for $NPR = 2.36, 3.72$ and 5.08 at all z/d for the elliptical and circular orifice. It is characterized by—(a) symmetry in distribution, (b) value of at stagnation point, (c) presence of the local minima. The recovery factor is almost symmetrically distributed along the major and minor axes of the elliptical orifice for all NPR at all z/d . For lower $z/d = 2$

for moderately underexpanded jets the recovery factor distribution is similar for circular and elliptical orifice. For highly underexpanded jets due jets instability the distribution is non uniform. The recovery factor distribution shows that at the stagnation point recovery factor value remains at around 0.9 after that a steep decrease (around 15 %) in recovery factor is observed till around $1.5 r/d$ for $z/d = 2$. This decrease in the recovery factor may be attributed due to the presence of vortex ring around the edge of stagnation

Fig. 16 Recovery factor distribution for different NPR

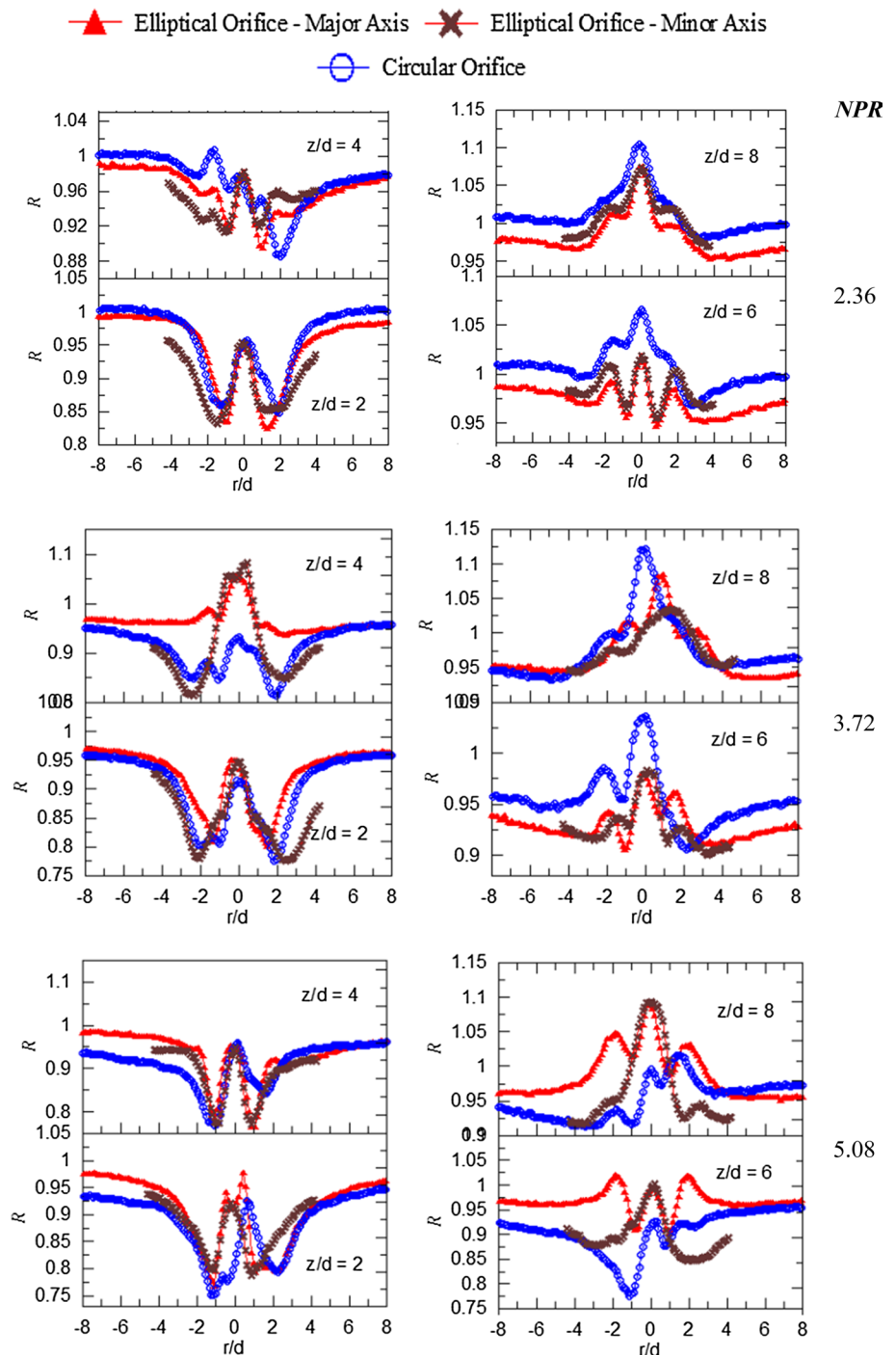
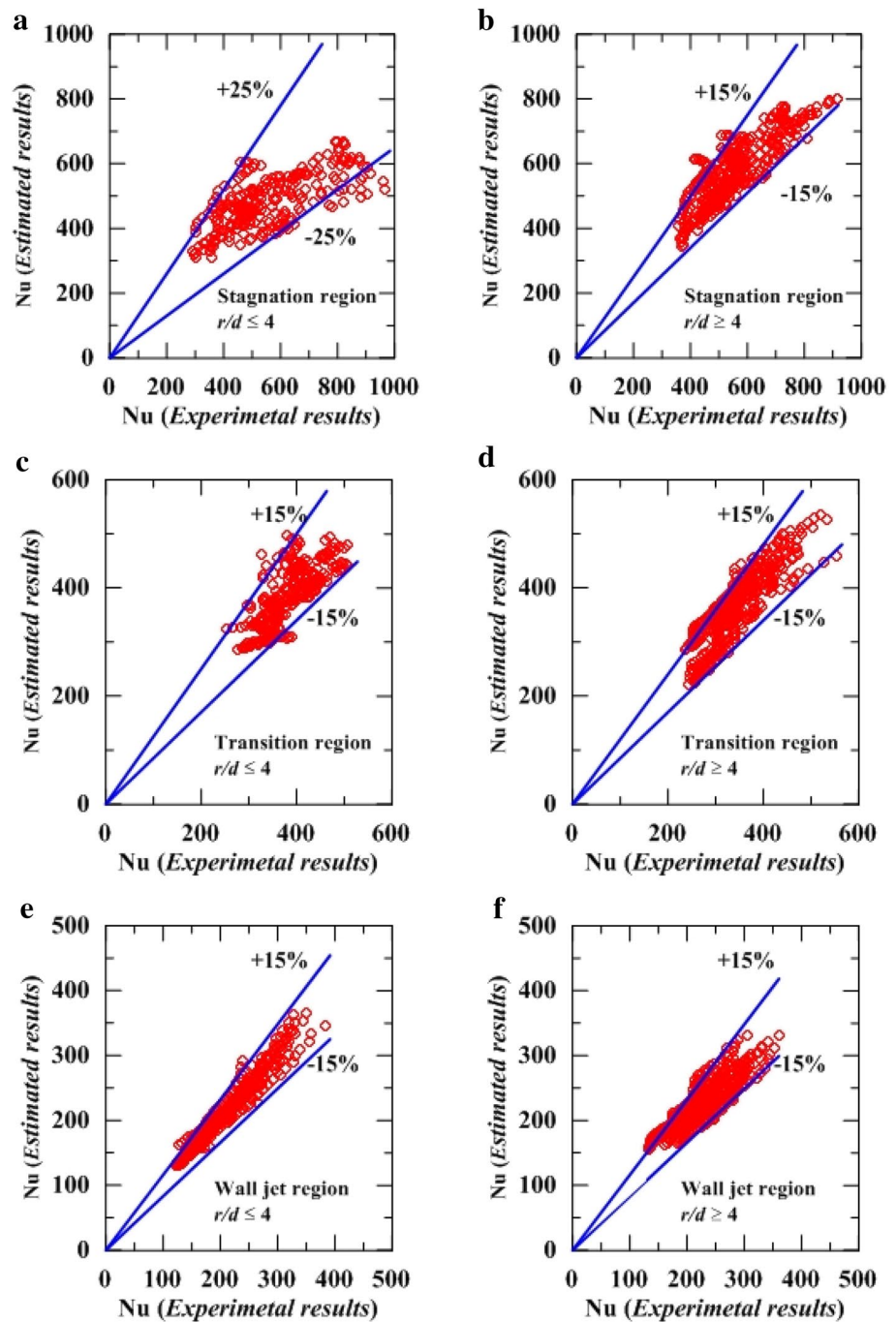


Fig. 17 Comparison between Nusselt number measured experimentally and Nusselt number estimated from correlations



region as reported by Kim et al. [15, 16] and Yu et al. [17]. Due to temperature separation at centre of this vortex ring, recovery factor decreases. In the transient region due to turbulent mixing in the transition region, recovery factor increases uniformly. It is also observed that the local minima position in the recovery factor distribution is dependent on the shape of the orifice. With the increase in z/d , due to mixing and viscous dissipation over the surface, the recovery factor increases up to unity as shown in Fig. 16.

4 Correlations for the heat transfer distribution

The local Nusselt number distribution for circular and elliptical orifice shows similar distribution for both orifice jets. Although it is inferred that elliptical orifice jets provide lower heat transfer rates compared to circular, but the variation is within uncertainty limits. The local Nusselt number can be predicted based on correlations for stagnation, transition and wall jet region.

4.1 Local heat transfer in stagnation region ($r/d \leq 1$)

From local Nusselt number distribution for z/d ($2 \leq z/d \leq 8$), it is observed that for the range of NPR covered in present study, Nusselt number distribution are similar for $z/d \geq 4$. Local Nusselt number graph shows bell shape distribution for $z/d \geq 4$, which are comparable to the distribution reported for incompressible jets by Katti and Prabhu [22]. They proposed correlations (Eq. 11) for local Nusselt number distribution in the stagnation region (for $z/d = 0.5$ –8) for incompressible jets.

$$Nu = a_1 Re^{0.5} Pr^{0.33} \left(\frac{z}{d}\right)^{-0.11} \left[1 - \frac{\left(\frac{r}{d}\right)^2 \left(\frac{z}{d}\right)^{-0.2}}{b_1}\right]^{1.2} \quad (11)$$

The coefficients reported by Katti and Prabhu [22] underpredict the local Nusselt number in the range of -60 to -25 % of present experimental results. Table 3 reports modified coefficients based on present experimental results, which can predict the local Nusselt number within 25 % for $z/d \leq 4$ and within 15 % for $z/d \geq 6$ in the stagnation region. Figure 17 a, b shows comparison of experimentally measured ‘Nu’ and estimated ‘Nu’. It may be concluded that for $z/d \geq 6$, local heat transfer from compressible jets can be well predicted by incompressible jets correlation proposed by Katti and Prabhu [22]. This may be attributed to similar velocity profiles for both incompressible and compressible jets for $z/d \geq 6$, where jets are fully expanded. However, for $z/d \leq 4$, due to highly non uniform distribution and presence of shocks for compressible jets, present correlations do not show good agreement (± 25 %) with the experimental results.

4.2 Local heat transfer in transition region ($1 \leq r/d \leq 3.5$)

It is observed that for compressible underexpanded jets, transition region is spread from 1 to 3–3.5d from stagnation point compared to that for incompressible jets for up to 2.5 nozzle diameters. In the transition region ($1 \leq r/d \leq 3.5$), the correlation reported by Katti and Prabhu [22] underpredict local Nusselt number in the range of -25 to -60 % with respect to present experimental results. In the present study, the correlations are modified based on experimental results, for $z/d \leq 4$ Eqs. 12 and 13 predict local Nusselt number within ± 15 % of the experimental results as shown in Fig. 17 c, d.

Table 3 Coefficient a_1 and b_1

z/d	2	4	6	8
a_1	2.5	3.2	3.3	3.1
b_1	4.3	2.7	2.9	2.7

Table 4 Enhancement coefficient

z/d	2	4	6	8
‘E’ from Katti and Prabhu [22]	2.6	2.4	2.35	2.3
Modified ‘E’	3.4	2.9	2.8	2.6

$$Nu = 1.846 Re^{0.52} \left(\frac{z}{d}\right)^{-0.1724} \left(\frac{r}{d}\right)^{-0.3767} \quad \text{for } z/d \leq 4 \quad (12)$$

$$Nu = 2.203 Re^{0.52} \left(\frac{z}{d}\right)^{-0.2433} \left(\frac{r}{d}\right)^{-0.4807} \quad \text{for } z/d \geq 6 \quad (13)$$

4.3 Local heat transfer in wall jet region ($r/d \geq 3.5$)

Wall jet region exist beyond $r/d \geq 3.5$, where the boundary layer becomes turbulent. In this region, the Nusselt number can be predicted by Eq. 14, as suggested by Katti and Prabhu [22]. The enhancement coefficient (E) reported by Katti and Prabhu [22] as reported in Table 4, underpredicts the local Nusselt number by -25 % in comparison with the present experimental results. In the present study, this enhancement coefficient (E) is modified as reported in Table 4, which predicts local Nusselt number within ± 15 % (Fig. 17 e, f) of experimental results for $r/d \geq 3.5$ and $2 \leq z/d \leq 8$.

$$Nu = 0.0436(E) Re^{0.8} Pr^{0.33} \left(\frac{z}{d}\right)^{0.0976} \left(\frac{r}{d}\right)^{-1.0976} \quad (14)$$

5 Conclusions

The impact pressure distributions, shadowgraphs and heat transfer characteristics of the asymmetric and axisymmetric orifices are compared. Following conclusions may be drawn from the present study:

- The pressure drop across the elliptical orifice is more than the circular orifice. The expansion of the air just outside the orifice takes place in elliptical orifice with a slower rate than the circular orifice. But as the axial distance increases, the expansion of the air takes place much faster in elliptical orifice than the circular orifice. The pressure reaches almost to atmospheric pressure at $z/d = 16$ in case of the elliptical orifice at all NPRs. For the circular orifice, the pressure at the axial location of $z/d = 16$ is slightly higher for $NPR = 2.36$ than that exists for $NPR = 5.08$. The pressure drops with cyclic fluctuations along the axis of the elliptical orifice. The pressure in radial direction for the elliptical orifice is always less than that for the circular orifice.
- Shadowgraphs show that the plate shocks exists for higher NPR ($NPR \geq 3.72$) for nozzle to plate distances up to four. The shock cell present in the fluid flow locally influences the heat transfer.

- The differences in the local Nusselt number occurs close to the stagnation point and not in the wall jet region where it follows a self similar profile. The greater expansion rates in the radial and the axial directions, higher mixing and entrainment of the ambient air do not contribute to enhance the convective heat transfer coefficients for the elliptical orifice.
- The circular orifice has better performance in convective heat transfer than the elliptical orifice, in general, at all z/d and all NPR . The performance of the circular orifice is far better at $z/d = 2$ than at any other z/d ; as an average 7 % higher values of the average Nusselt number. For $NPR = 5.08$, the elliptical orifice has better heat transfer coefficients (4 % higher) than that for the circular orifice for $z/d \geq 4$.
- Axis switching is observed for the elliptical orifice and not for the circular orifice. The axis switching has altered the temperature distribution over the target plate. This gives rise to steeper thermal gradients across the jet section in case of elliptical orifice.
- Local heat transfer can be predicted with the suggested correlations comparable within 15 % to the experimental results.

Acknowledgments Authors acknowledge the efforts put in by Mr. Vittoba Kharat and Mr. Rahul Shirsat in building the experimental setup and fixing the mechanical problems during the course of the experiments.

References

- Henderson LF (1966) Experiments on the impingement of a supersonic jet on a flat plate. *J Appl Math Phys* 17(5):553–569
- Donaldson CD, Snedeker RS (1971) “A study of free jet impingement. Part 1. Mean properties of free and impinging jets.”. *J Fluid Mech* 45(02):281–319
- Lamont PJ, Hunt BL (1980) “The impingement of underexpanded, axisymmetric jets on perpendicular and inclined flat plates”. *J Fluid Mech* 100(3):471–511
- Addy AL (1981) Effects of axisymmetric sonic nozzle geometry on Mach disk characteristics. *AIAA J* 19(1):121–122
- Mehta RC, Prasad JK (1998) Investigation of supersonic free jets emanating from convergent divergent nozzles. *Int J Comput Fluid Dyn* 10:61–71
- Alvi FS, Ladd JA, Bower WW (2002) Experimental and computational investigation of supersonic impinging jets. *AIAA J* 40(4):599–609
- Inman JA, Danehy PM, Nowak RJ, Alderfer DW (2008) “Fluorescence imaging study of impinging underexpanded jets”. AIAA- 2008-619, 46th AIAA Aerospace Sciences Meeting and Exhibit, Nevada
- Thangadurai M, Das D (2010) Characteristics of counter-rotating vortex rings formed ahead of a compressible vortex ring. *Exp Fluids* 49(6):1247–1261
- Thangadurai M, Das D (2012) Experimental study on a compressible vortex ring in collision with a wall. *J Vis* 15(4):321–332
- Rajapukeran E (1993) “Experimental and computational investigations of underexpanded jets from elliptical sonic nozzles”, Ph. D. Thesis, Indian Institute of Science, Bangalore, India
- Yaga M, Ueda K, Ohshiro T, Senaha I, Oyakawa K (2000) Experimental and three-dimensional numerical study on under-expanded impinging jets. *J Therm Sci* 9(4):316–321
- Jothi TJS, Srinivasan K (2008) Acoustic characteristics of non-circular slot jets. *Acta Acust United Acust* 94:229–242
- Srinivasan K, Jothi TJS, Shet USP, Elangovan S, Rathakrishnan E (2009) “Relationship between shock-cell length and noise of jets from rectangular and elliptical nozzles”. *Int J Turbo Jet Engines* 26:145–153
- Rahimi M, Owen I, Mistry J (2003) Impingement heat transfer in an under-expanded axisymmetric air jet. *Int J Heat Mass Transf* 46:263–272
- Kim BG, Yu MS, Cho HH (2003) Recovery temperature measurement of underexpanded sonic jets impinging on a flat plate. *J Thermophys Heat Transf* 17(3):313–319
- Kim BG, Yu MS, Cho YI, Cho HH (2002) Distributions of recovery temperature on flat plate by underexpanded supersonic impinging jet. *J Thermophys Heat Transf* 16(3):425–431
- Yu MS, Kim BG, Cho HH (2005) Heat transfer on flat surface impinged by an underexpanded sonic jet. *J Thermophys Heat Transf* 19(4):448–454
- Ramanujachari V, Vijaykant S, Roy RD, Ghanegaonkar PM (2005) Heat transfer due to supersonic flow impingement on a vertical plate. *Int J Heat Mass Transf* 48:3707–3712
- Meena HC, Reodikar SA, Vinze R, Prabhu SV (2016) Influence of the shape of the orifice on the local heat transfer distribution between smooth flat surface and impinging incompressible air jet. *Exp Therm Fluid Sci* 70:292–306
- Vinze R, Chandel S, Limaye MD, Prabhu SV (2016) Influence of jet temperature and nozzle shape on the heat transfer distribution between a smooth plate and impinging air jets. *Int J Therm Sci* 99:136–151
- Lytle D, Webb BW (1994) Air jet impingement heat transfer at low nozzle plate spacings. *Int J Heat Mass Transf* 37:1687–1697
- Katti V, Prabhu SV (2008) Experimental study and theoretical analysis of local heat transfer distribution between smooth flat surface and impinging air jet from a circular pipe nozzle. *Int J Heat Mass Transf* 51:4480–4495
- Moffat RJ (1988) Describing the uncertainties in experimental results. *Exp Therm Fluid Sci* 1:3–17
- Quinn WR (2006) Upstream nozzle shaping effects on near field flow in round turbulent free jets. *Eur J Mech B/Fluids* 25(3):279–301
- Jothi TJS, Srinivasan K (2009) Role of initial conditions on noise from underexpanded pipe jets. *Phys Fluids* (1994–present) 21(6):66–103
- Iwamoto J, Deckker BEL (1981) Development of flow field when a symmetrical under-expanded sonic jet impinges on a flat plate. *J Fluid Mech* 113:299–313